Available online at www.sciencedirect.com

SCIENCE DIRECT®

Nuclear Instruments and Methods in Physics Research A 550 (2005) 217–240

NUCLEAR INSTRUMENTS & METHODS IN PHYSICS RESEARCH
Section A

www.elsevier.com/locate/nima

# The COMPASS trigger system for muon scattering☆

C. Bernet[a,1], A. Bravar[a,2], J. Hannappel[b], D.v. Harrach[a], R. Hermann[a], E. Kabuß[a,*], F. Klein[b], A. Korzenev[a,3], M. Leberig[a,2], M. Ostrick[b], J. Pretz[b], R. Windmolders[b], J. Zhao[a]

[a] *Institut für Kernphysik, Mainz University, 55099 Mainz, Germany*
[b] *Physikalisches Institut, Bonn University, 53115 Bonn, Germany*

Received 3 January 2005; received in revised form 10 May 2005; accepted 10 May 2005
Available online 6 July 2005

**Abstract**

The trigger system of the COMPASS experiment at the CERN polarized muon beam is presented. It detects muon scattering events on (polarized) nucleons with a relative energy loss exceeding a selectable value $y_{\min}$ independent of the four-momentum transfer. The requirement of a minimum energy deposit in a hadron calorimeter rejects background events like scattering on electrons, elastic and quasi-elastic radiative events as well as events from beam halo tracks. The trigger system which can be considered as a tagger for quasi-real photon events is now, along with larger trigger hodoscope system for deep inelastic scattering events, in regular use for the measurement of the gluon polarisation $\Delta G/G$.

*PACS:* 13.85Hd; 29.30.Aj; 29.40.Mc; 29.40.Vj

*Keywords:* Polarised deep inelastic lepton scattering; Muon beam; COMPASS spectrometer; Trigger; Scintillators; Calorimeter

## 1. Introduction

Fixed target scattering experiments with muons in the energy range of $E = 50-500\,\text{GeV}$ have made significant contributions to the understanding of QCD and the partonic structure of hadrons [1,2]. The EMC and SMC collaborations [3,4] made use of the natural high degree of muon polarisation in scattering experiments on solid state polarised targets to study the spin structure of nucleons. Experiments with polarised muon beams are still unique in covering the low Bjorken-$x$ region of the spin structure functions. Up to now only the lepton beams are polarised in ep-colliders. In addition, the large duty cycle of muon beams is

---

☆Supported by the Bundesministerium für Bildung und Forschung.

*Corresponding author.
*E-mail address:* emk@kph.uni-mainz.de (E. Kabuß).

[1] Now at CERN, Geneva, Switzerland.

[2] Now at BNL, Upton, USA.

[3] On leave from JINR, Dubna.

doi:10.1016/j.nima.2005.05.043

essential to measure the produced hadrons in coincidence.

The main aim of the initial phase of the COMPASS experiment is a measurement of the gluon polarisation $\Delta G/G$. Access to the gluon distribution is provided by the photon gluon fusion process which can be tagged by either the production of open charm or by a hadron pair with high transverse momentum.

Throughout this paper the following kinematic variables will be used: $E$ ($E'$) is the energy of the incoming (scattered) muon, $M_N$ the nucleon mass, $m$ the muon mass, $m_c$ the charm quark mass, $\theta$ the muon scattering angle in the laboratory system, $Q^2$ the negative squared four-momentum of the virtual photon, $v = E - E'$ its energy in the laboratory system, i.e. the energy loss of the muon, $y = v/E$ the fractional energy loss and $x_{Bj} = Q^2/2M_N v$ the Bjorken scaling variable. The center of mass energy squared, $\hat{s}$, is given by the four-momenta of the photon, $p_\gamma$, and the gluon, $p_g$ in the photon-gluon subsystem, $\hat{s} = (p_\gamma + p_g)^2$.

The COMPASS experiment makes use of all the features of previous deep inelastic muon scattering spin experiments. Its main additional feature is the use of the full range of $Q^2$, including the quasi-real photon range $Q^2_{\min} \approx m^2y^2/(1-y) < Q^2 \lessapprox 0.5\,\mathrm{GeV}^2$. This range is usually disregarded in inclusive deep inelastic lepton scattering (DIS) experiments since the perturbative QCD description fails at low $Q$ due to the absence of a hard scale. This is not the case in the photon gluon fusion process where a hard scale is provided by the center of mass energy $\sqrt{\hat{s}}$ of the photon–gluon system. The quasi-real photon energy spectrum has a $1/v$ shape similar to Bremsstrahlung. It is only useful for charm production above a minimum photon energy $v_{\min}$ or alternatively $y_{\min} = v_{\min}/E$ as $\hat{s} \approx 2vM_N \cdot x_g > 4m_c^2$ is required. This corresponds to a photon energy $v > 45\,\mathrm{GeV}$ for a momentum fraction of the gluon $x_g < 0.1$. Not only the energy of the virtual photon, $v$, is of importance but also the polarisation transfer, $D(y)$, approximately proportional to $y$. A beam energy of 160 GeV was chosen as a compromise between a high photon flux and a high polarisation in order to maximize the statistical significance of the $\Delta G$ measurement.

The trigger system for processes induced by quasi-real photons has to select events with

(1) a very small $Q^2$, corresponding to muon scattering angles down to $\theta = 0\,\mathrm{mrad}$,
(2) an energy loss $v > 45\,\mathrm{GeV}$,
(3) forward hadrons in the final state.

The deep inelastic scattering range with $Q^2 > 0.5\,\mathrm{GeV}^2$ can be covered by an additional trigger system using only information from the scattered muon, similar to the ones used in previous muon experiments [5].

The next two sections give a short description of the muon beam and the COMPASS experiment and introduce the new concept of the trigger system. A detailed description of this system is given in Section 4 and the results from the 2003 data taking are presented in Section 5. More detailed technical information is available in Ref. [6].

## 2. The COMPASS experiment

The COMPASS experiment [7] is performed at the M2 muon beamline of the CERN SPS. The muon beam is produced from the SPS 400 GeV proton beam by the decay of $\pi$- (and K)-mesons emerging from a primary Be target. Part of the mesons decay in flight into muons which are guided by a FODO section to the experimental area. The muon beam acquires a natural polarisation due to the weak $\pi$ and K decays. The polarisation can be chosen by selecting a specific ratio of the parent pion to decay muon momentum. Typical polarisation values of about 80% can be obtained at beam intensities of $2 \times 10^8$ muons per spill with energies between 100 and 200 GeV. The spill length is 4.8 s out of the 16.8 s cycle time.

The momentum of each incoming muon is measured upstream the experimental area with the help of a beam momentum station consisting of 5 planes of scintillator strips interleaved with a dipole magnet. The tertiary nature of the muon beam results in a sizeable beam emittance. The beam is focussed at the target to a sigma of 7 mm for the Gaussian core. It has a divergence of about

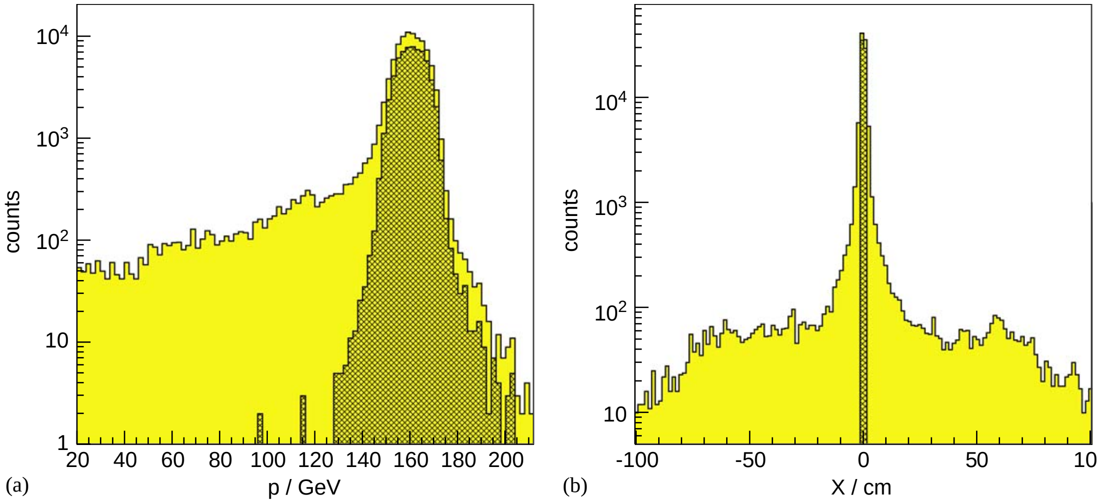

Fig. 1. (a) Momentum distribution and (b) horizontal profile at the target center for incoming particles obtained with a random trigger. The shaded areas correspond to particles passing through both target cells.

1 mrad and a momentum spread of $\sigma_p/p \approx 5\%$. Fig. 1a shows the measured momentum distribution for incoming muons from a sample of events taken with a random trigger and reconstructed in the spectrometer; Fig. 1b shows the spatial distribution at the target center for the same events. The Gaussian core and the non-Gaussian tail, called "near halo", which amounts to about 30% of the core intensity, are clearly visible. There is also a considerable contribution of lower energy muons at larger distances from the beam which is called "outer halo" [8].

The layout of the COMPASS experiment is shown in Fig. 2. The trajectories of the incoming particles are measured in a series of scintillating fibre planes and silicon detectors interleaved with veto hodoscopes which are used for trigger purposes. The muons are scattered off a polarised solid state target located inside a superconducting solenoid [9]. It consists out of two 60 cm long cells filled with $^6$LiD. The two cells, separated by 10 cm, are polarised in opposite directions and are immersed in a bath of a $^3$He/$^4$He mixture. The scattered muons and the forward produced hadrons are detected in a large acceptance two stage spectrometer. A large gap 1 Tm dipole magnet with a vertical magnetic field (SM1) is used in the first stage to measure low momentum tracks, mainly of hadrons produced in the target, whereas in the second stage a 4.4 Tm dipole magnet (SM2), bending the particles in the same direction as the first one, is used for the scattered muons and other high momentum particles. A large number of tracking detectors determine the trajectories with high precision. Both stages use hadronic calorimetry and absorber walls ("muon filter") for hadron and muon identification. In addition a RICH detector located in stage 1 is used for $\pi$/K/p separation in the momentum range up to 50 GeV [10]. Most of the trigger hodoscopes are located at the end of the spectrometer behind the second muon filter.

## 3. The trigger for quasi-real photoproduction

The measurement of polarised quasi-real photoproduction for the determination of $\Delta G$ requires a trigger system which can detect scattered muons with a given minimum energy loss at scattering angles down to zero. There are a number of background processes, such as elastic scattering off target electrons and elastic and quasi-elastic radiative scattering off target nuclei present in the kinematical region of quasi-real photoproduction. For the suppression of the background we make

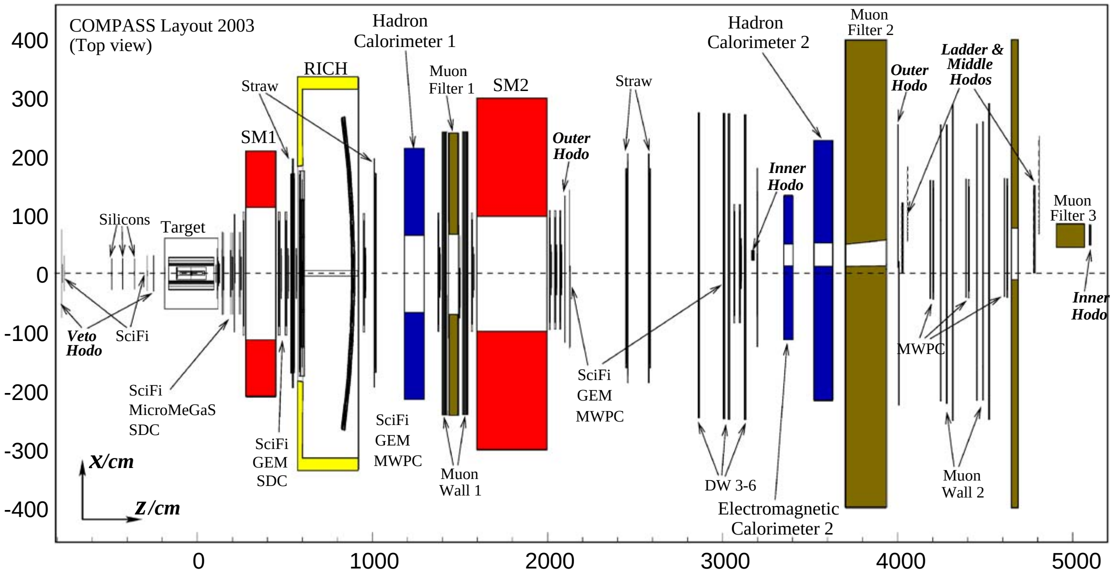

Fig. 2. Schematic drawing of the COMPASS experiment. Shown is the 2003 setup.

use of the fact that no forward hadrons are associated to those events. Thus, hadronic calorimeter information can be used to reject most of the background events and those triggered by beam halo.

The trigger system has to serve several purposes: to select event candidates in a high rate environment with a decision time below 500 ns at minimum dead time, to provide precise event times for unambiguous association with incident beam muons and to generate strobes for gating of detectors for fast muon correlated pulse height analysis. The requirements of efficiency and purity are generally in conflict and demand an optimisation depending on the relevant physics processes and the maximum tolerable trigger rate as given by the event size and the bandwidth limit (30 Mb/s) of the central data recording system.

### 3.1. Triggering on energy loss

The energy loss trigger uses the muon track direction behind the two magnets in the bending plane of the dipole spectrometer. The system consists of two vertical hodoscope planes (H4 and H5) at distances of $z_1$ and $z_2$ from the target, measuring the horizontal positions $x_1$ and $x_2$ of the deflected track. For an isolated muon track originating from the target this information is sufficient to determine the horizontal component of its scattering angle $\theta_x$ and its momentum $p'$, i.e. $y$ for a fixed beam momentum. In the small angle approximation the magnets provide a transverse kick of $\Delta p_x/\mathrm{GeV} = 0.3 \int B\,\mathrm{d}l/\mathrm{Tm}$ at the effective bending position $z_\mathrm{m}$. The inverse scattered muon momentum is a linear combination of the two measured positions $x_1$ and $x_2$ given by the following relation where all other quantities are known:

$$\frac{\Delta p_x}{p'} z_\mathrm{m} = \frac{x_1 \cdot z_2 - x_2 \cdot z_1}{(z_2 - z_1)}. \tag{1}$$

The trigger for a scattered muon with a momentum below a preselected value $p'_\mathrm{max}$ is then realized by requiring a coincidence of elements $x_1$ and $x_2$ in the hodoscopes positioned at $z_1$ and $z_2$ fulfilling the condition in Eq. (1) (see Fig. 3). Up to the beam energy spread this corresponds to an energy loss larger than $v_\mathrm{min} \geqslant p - p'_\mathrm{max}$.

Under realistic conditions, with a beam of finite emittance and momentum spread and a target of finite length $L$, the only additional parameter is the impact parameter $x_0$, which is the $x$-coordinate of the undeflected scattered track at the target centre $z_0 = 0$:

$$\frac{\Delta p_x}{p'} z_{\mathrm{m}} = x_0 - \frac{x_1 \cdot z_2 - x_2 \cdot z_1}{(z_2 - z_1)}. \tag{2}$$

Since $x_0$ is not available for the trigger decision it introduces an uncertainty in the momentum determination. For beam muons within the finite target radius $r_0$ and target length $L$ $x_0$ is limited by

$$|x_0| < r_0 + \frac{L}{2}\theta_x^{\max}. \tag{3}$$

With a target radius of 1.5 cm, a target length of $L = 1.3\,\mathrm{m}$ and $\theta_x^{\max} = 5\,\mathrm{mrad}$ we arrive at an error $\delta x_0 = 9\,\mathrm{mm}$ taking the known beam parameters into account.

The momentum resolution is then given by

$$\begin{aligned}\frac{\delta p'}{p'} &= \frac{p'}{\Delta p_x \cdot z_{\mathrm{m}}} \\ &\quad \times \sqrt{\delta x_0^2 + \left(\frac{z_2}{z_2 - z_1}\right)^2 \cdot \delta x_1^2 + \left(\frac{z_1}{z_2 - z_1}\right)^2 \cdot \delta x_2^2} \\ &= \frac{\delta y}{1 - y}.\end{aligned} \tag{4}$$

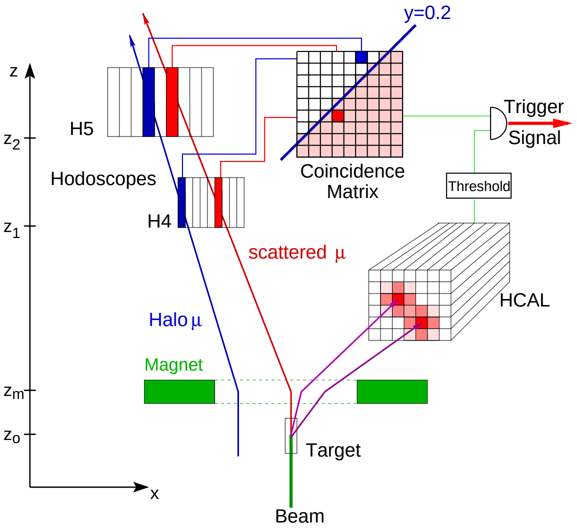

Fig. 3. Concept of the trigger for quasi-real photoproduction with high energy loss. The scattered muon leads to a coincidence in the activated area of the coincidence matrix while the halo muon fails. In addition, a minimum hadron energy can be required in the calorimeter.

If the element width of the hodoscopes at $z_1$ and $z_2$ is chosen proportional to their distance from the target, e.g. $\delta x_1 = 6\,\mathrm{mm}/\sqrt{12}$ at $z_1 = 32\,\mathrm{m}$ and $\delta x_2 = 11\,\mathrm{mm}/\sqrt{12}$ at $z_2 = 51\,\mathrm{m}$, then the three contributions to the momentum error $\delta p'$ are of similar size. With 5.4 Tm bending power at $z_{\mathrm{m}} = 15\,\mathrm{m}$, we arrive at $\delta p'/p' \approx 5.3\%$ or equivalently a resolution of $\delta y = 0.041$ at $y \approx 0.2$.

Additional effects on the sharpness of the cut in $y$ originate from the momentum spread of the beam and the effects of multiple scattering. Due to the momentum width $\delta p_0/p_0$ of the muon beam, cutting on $p'$ will introduce an error on $y = (p_0 - p')/p_0$ of $\delta y = (\delta p'^2/p_0^2 + p'^2 \delta p_0^2/p_0^4)^{1/2}$. The second term increases the error on $y$ to $\delta y = 0.055$. This would mean that a cut set at $y = 0.2$ would give full efficiency ($>95\%$) for $y > 0.31$ and full suppression ($<5\%$) for $y < 0.09$.

The selection of muon tracks requires an absorber in front of one of the two hodoscopes in order to reject hadron and electron tracks. The effects of multiple scattering on the measured track position are minimized if the absorber is placed directly in front of the second hodoscope. An absorber of 1.6 m of iron corresponding to 91 radiation lengths is chosen. All detectors between the two hodoscopes (calorimeter, lead wall, concrete absorbers, muon wall) have a hole in the center that matches the projected size of the trigger hodoscopes H4 and H5 (see Fig. 5). Typically at $p' = 0.7 \times 160\,\mathrm{GeV} = 112\,\mathrm{GeV}$ the multiple scattering leads to an rms width of $\delta\theta_x = 1.2\,\mathrm{mrad}$. The short distance of the second hodoscope to the center of the absorber only leads to an additional resolution effect of about 0.6 mm which is insignificant in view of the element width.

Obviously a fine grained structure of the hodoscopes at $z_1$ and $z_2$ and a muon filter very close to $z_2$ are needed only for combinations of $x_1$ and $x_2$ corresponding to the $y$ region of $y \approx 0.2$ where the cut has to be applied. Thus, the trigger system for the quasi-real photon events with $y > 0.2$ is divided into two parts. The region $0.2 < y < 0.5$ is covered by the inner system with the hodoscopes H4I and H5I described above. For large values of $y$, a coarse grained system with both hodoscopes (H4L and H5L) shielded by a hadron absorber can be used. As shown in Fig. 4

this is done with the so called ladder system. More details are given in Table 1.

### 3.2. Triggering on calorimetry

Events with a hadron in the final state can be selected by requiring a cluster with an energy deposition well beyond the value expected for a single muon in at least one of the hadron calorimeters. The typical cluster size of a hadron is of order of the interaction length (i.e. several tens of cm) while a muon is characterized by an energy deposition localized along its track. In order to correlate an energy deposition with a scattering event on the trigger level the time resolution and the integration time of the calorimeter are of great importance.

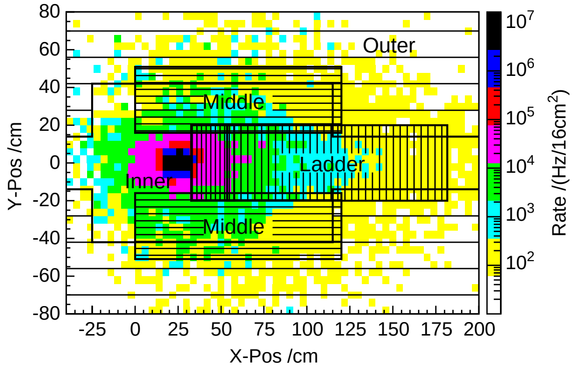

Fig. 4. MC-simulation of the muon rates per 16 cm$^2$ and s behind the muon filter 2 ($z = 40$ m). The sizes of the different hodoscope subsystems are indicated.

As shown in the schematic layout in Fig. 2 there are two large hadron calorimeters. Both consist of sandwiched iron-scintillator calorimeter modules with wavelength shifter and photomultiplier readout. They are shielded against electrons and photons either by lead or by the electromagnetic calorimeters. The requirement of a minimum energy deposition in the hadron calorimeters, well beyond the energy loss of a muon passing the calorimeter, rejects the background events mentioned above.

In practice the trigger has to deal with the very high rate of halo muons of $2 \times 10^7$/s passing through the calorimeter depositing an energy of

Table 1
The trigger hodoscopes and their main parameters

| System | Hodoscope | No. of strips | Width (mm) | Overlap (mm) | $z$-Pos. (m) | Area ($x \times y$) (cm$^2$) | Photomultiplier type |
|---|---|---|---|---|---|---|---|
| Inner | H4I (up) | 32 | 6 | 0.6 | 32 | 17.34 × 32 | 1 × R7400 |
| | H4I (dn) | 32 | 6 | 0.6 | 32 | | 1 × R7400 |
| | H5I (up) | 32 | 12 | 1 | 51 | 35.3 × 51 | 1 × XP2900 |
| | H5I (dn) | 32 | 12 | 1 | 51 | | 1 × XP2900 |
| Ladder | H4L | 32 | 22–67 | 1–3 | 40.65 | 128.2 × 40 | 2 × XP2900<br>2090, 2020 |
| | H5L | 32 | 27–87 | 1–3 | 48.05 | 168.2 × 47.5 | 2 × XP2900<br>2090, 2020 |
| Middle | H4MV (up) | 20 | 62 | 1.5 | 40.3 | 120 × 102 | 1 × XP2072B |
| | H4MV (dn) | 20 | 62 | 1.5 | 40.3 | | 1 × XP2072B |
| | H4MH | 32 | 21.5–25 | 1.5 | 40.4 | | 2 × XP2900 |
| | H5MV (up) | 20 | 77 | 1.5 | 47.7 | 150 × 120 | 1 × EMI9954B |
| | H5MV (dn) | 20 | 77 | 1.5 | 47.7 | | 1 × EMI9954B |
| | H5MH | 32 | 25–30 | 1.5 | 47.8 | | 2 × XP2900 |
| Outer | H3O | 16 | 70 | 5 | 23 | 200 × 100 | 2 × EMI9813B |
| | H4O | 32 | 150 | 10 | 40.0 | 480 × 225 | 2 × XP2020,<br>EMI9813B |

The last column also indicates whether the strips are read out on one or both ends. The overlaps between neighbouring strips guarantee high trigger efficiency.

typically 1.8 GeV ( see Fig. 17). The pulse length of an sandwiched iron-scintillator with wavelength shifter readout is of order 50 ns. Therefore the probability for a two muon pile-up is of order one. The problem can be alleviated by requiring at least one local cluster with an energy exceeding that of a single muon. The size of an energy cluster corresponding to a hadron is of order of one interaction length squared i.e. typically $20 \times 20\,\mathrm{cm}^2$. With a suitable cluster forming and processing hardware the pile-up problem can be reduced by more than a factor 10. Obviously this requirement is different from the requirement of a minimum hadronic energy. We have calculated the efficiency of such a trigger as a function of the total hadronic energy. We find that the efficiency is higher than 90% at the total energy larger than 5 times the threshold value. With a threshold at 5.4 GeV, which suppresses the single muon response by more than 90% we get more than 90% efficiency at $E_{\mathrm{had}} = \nu = 30\,\mathrm{GeV}$. In order to form the combined trigger the cluster signal has to be correlated to the hodoscope signal. A good time resolution of order of 1 ns of the calorimeter is necessary to reduce the number of accidental coincidences. The calorimeter trigger can work in coincidence with any of the geometrical triggers.

## 4. The trigger system

This chapter describes the hardware realisation of the full trigger system, including the DIS triggers for events with $Q^2 > 0.5\,\mathrm{GeV}^2$. We also describe the veto system added to the trigger system in order to suppress events due to halo muons.

### 4.1. The hodoscopes

Fig. 4 shows the hit distribution of scattered muons behind muon filter 2 as obtained in a Monte-Carlo simulation. In view of the high rates in the central region the hodoscope system is subdivided into four parts. The *inner* and the *ladder* systems covering the quasi-real photon events have already been introduced in Section 3.

The *middle* system selects quasi-real photon events as well as deep inelastic scattering events. It uses two planes of the hodoscopes H4M and H5M to detect muons scattered with angles between 4 and 12 mrad by measuring the vertical projection, $\theta_y$, of the scattering angle in the non-bending plane and checking its compatibility with the target position ("vertical target pointing"). Two additional planes measure the horizontal projection $\theta_x$ and allow to perform a coarse energy cut. The *outer* system selects muons up to $Q^2 \approx 20\,\mathrm{GeV}^2$ by vertical target pointing. It consists of large area hodoscopes (H3O and H4O). The upper limit in $Q^2$ is fixed by the size of the gap in the second spectrometer magnet.

The inner, ladder and middle systems use vertical scintillator strips to measure the energy loss via the deflection in the bending plane. Horizontal scintillator strips are used in the middle and outer systems for vertical target pointing. The inner, ladder and outer systems thus consist of two and the middle system of four scintillator hodoscopes. The location of these hodoscopes in the COMPASS experiment is shown schematically in Fig. 5 and their characteristics are summarized in Table 1. Fig. 6 illustrates the grouping of hodoscopes in pairs and the corresponding trigger matrix patterns used during the data taking in 2003 (see Section 4.2).

Fig. 5 also shows the concrete and iron absorbers used to identify the muon tracks. In the ladder and the middle systems, a 2.4 m thick concrete absorber together with the material of the hadron calorimeter HCAL2 located in front of the first hodoscope, is used for muon filtering. Due to the large element width in the outer system

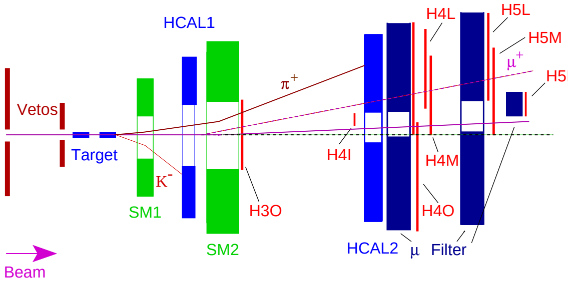

Fig. 5. Location of the components relevant for the trigger (schematically). For the true scale refer to Fig. 2 (see also Table 1).

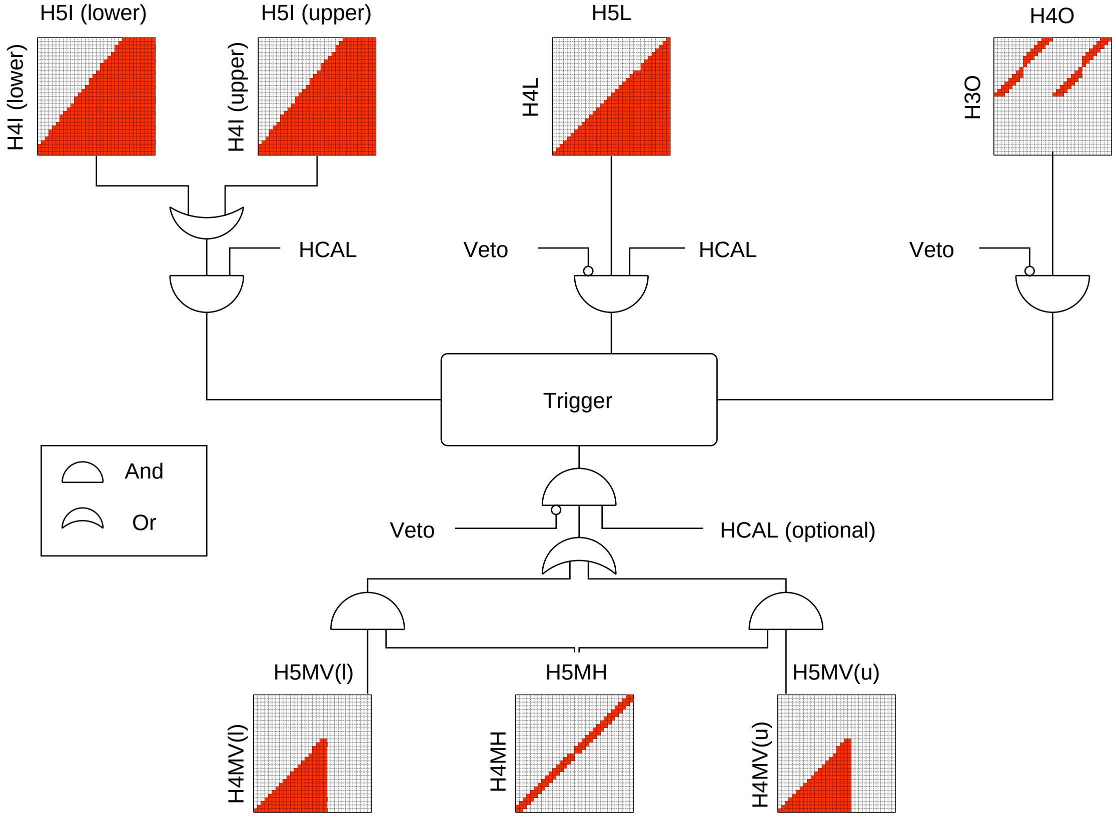

Fig. 6. Hodoscope combinations and matrix patterns used for data taking. The dark areas indicate enabled coincidences.

compared to the ladder and middle system a large lever arm is needed. Therefore the first hodoscope of the outer system, H3O, is installed directly behind the second spectrometer magnet. This hodoscope has a much larger central hole, covered by the other systems, to avoid excessive rates in the 7 cm wide strips.

### 4.1.1. *The inner system*

The requirements on rate capability and time resolution are most stringent for the hodoscopes of the inner system, H4I and H5I, which are therefore described in more detail [11]. These hodoscopes cover a small area (see Table 1) in a high flux environment. Vertical strips with a width of 6 and 12 mm in H4I and H5I, respectively, are used to measure the energy loss with the necessary resolution. In order to reduce the rate in the individual elements and also accidental coincidences the hodoscopes are split in two parts: above and below the bending plane. The vertical overlap of the two parts (16 mm for H4I and 9 mm for H5I) guarantees that a muon originating from the target volume passes either the two upper or the two lower planes.

Each half of the two hodoscopes consists of 32 strips staggered along the beam direction in 4 rows to cope with the diameter of the photomultipliers and to avoid the use of bent light guides (see Fig. 7). The hodoscopes were rotated by 18 mrad in the bending plane to compensate for the mean angle of deflection of the scattered muons. This guarantees angles of incidence close to 90 degrees. Horizontal overlaps of 0.6 and 1 mm between neighbouring strips were chosen to obtain full geometrical efficiency for a range of ±5 mrad with respect to the normal.

To achieve the best possible time resolution great care was given to the selection of the materials used to build the inner hodoscopes. A fast scintillator (Bicron BC404) with a high light output was selected to obtain clean muon signals above threshold. As this material is sensitive to external forces we use light guides glued to the scintillator material to fix the position of the scintillator. Diamond tool finish was chosen to provide high quality surfaces of the material. The light is read out by Hamamatsu R7400 (for H4I) and Philips XP2900 (for H5I) photomultipliers supplemented with active voltage dividers providing high rate capability. A modified version of the ones developed at the IPN Orsay for the MAMI A4 experiment [12] is used. The light coupling between the light guide and the photomultiplier (PM) is done with the help of a thin silicon disc. The strips are wrapped in aluminium foils to improve light collection and to prevent cross talk between neighbouring channels. The whole hodoscope is put into a light-tight box (see Fig. 7) with windows at the position of the muon beam and can be moved under remote control for fine adjustment and beam monitoring purposes. The front and back cover contain thin entrance and exit windows for the muon beam made of black plastic sheets.

Fig. 8 shows typical ADC spectra for a strip in H4I and H5I, obtained during test measurements in the muon beam. The pulse height distributions show a pedestal peak, a background region and a muon peak which is well described by a Landau distribution. Deviations at large pulse heights are

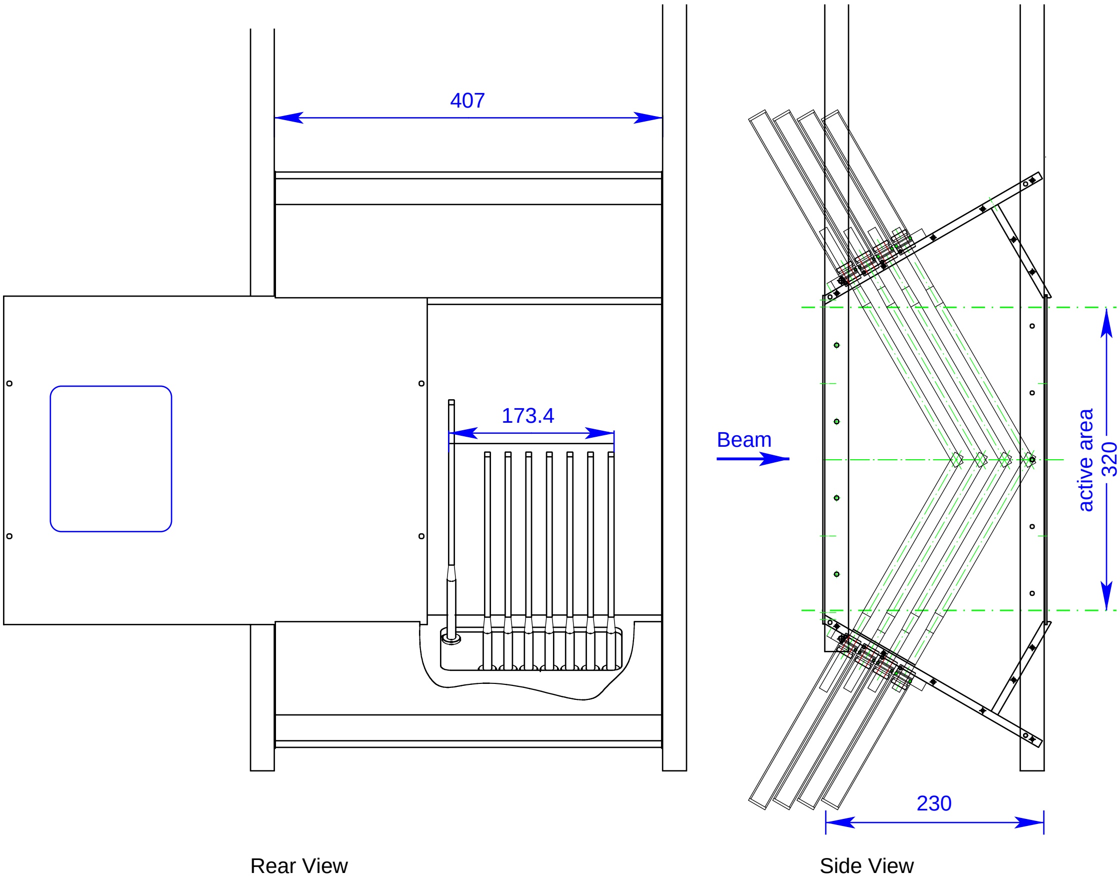

Fig. 7. Rear and side view of H4I. To allow free view onto the scintillators the cover is shifted to the left. Only some scintillators of the last and one of the first row are shown.

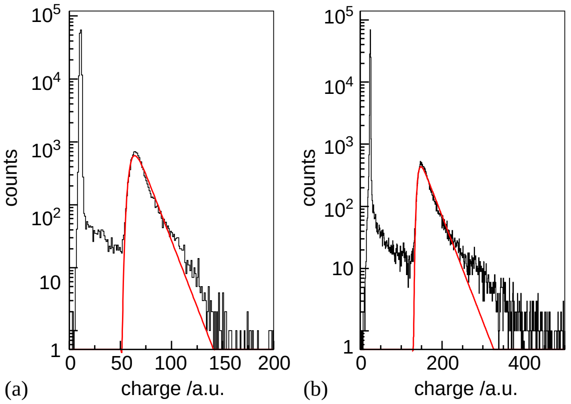

Fig. 8. ADC spectrum for a single strip in H4I and H5I obtained with the muon beam. The curves represent a fit with Landau distributions to the signal area.

due to double hits. The background between pedestal and signal is about a factor of 30 lower than the muon signal. It is due to delta electrons and muons passing through edges. Thresholds corresponding to 1/3 of the most probable muon signal were applied.

The scintillators are read out on one side only. For hodoscopes perpendicular to the beam direction ($\alpha = 0$) this results in a time difference $\Delta t$ between the signals from H4I and H5I depending on the slope of the particle track as illustrated in Fig. 9:

$$\begin{aligned}\Delta t &= T_5 - T_4 \\ &= \frac{z_5 - z_4}{c\cos\theta_y} + T_5^{\mathrm{lp}}(\theta_y) - T_4^{\mathrm{lp}}(\theta_y). \qquad (5)\end{aligned}$$

The dependence on the angle $\theta_y$ can be neglected in the first term of Eq. (5), but the difference in the propagation time $T_5^{\mathrm{lp}} - T_4^{\mathrm{lp}}$ is sizeable and can be up to 650 ps. To correct for this difference the strips of H4I have to be inclined by an angle $\alpha$ as shown in Fig. 9. The angle $\alpha$ was determined from the dependence of the propagation time on the distance to the PM as measured in a test beam. The measured relations were found to be non-linear and the best cancellation occurred with an inclination angle of 30°. The non-linearity is caused by the superposition of the light reflected at the far end and the light traveling directly to the PM, which distorts the shape of the signal and thus causes a time shift in the constant fraction discriminator (CFD).

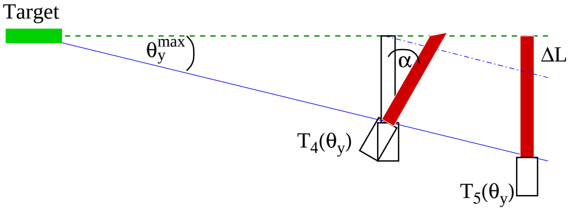

Fig. 9. Sketch of the time difference in H4I and H5I for elements read on one side only.

Fig. 10 shows the effect of the light propagation on the signal arrival time versus the angle $\theta_y$, as it has been measured with the final setup, i.e. with H4I already inclined. In Fig. 11a the time difference between the two hodoscope signals is plotted against $\theta_y$ demonstrating the compensation effect. The compensation is not perfect due to the non-linearities displayed in Fig. 10 and a slight mismatch of the inclination angle due to the fact that the test measurements were not performed with the final readout electronics. The contribution of the light propagation effect of 330 ps to the rms is about 100 ps and thus small compared to the observed distribution of time differences shown in Fig. 11b.

## 4.2. Hodoscope electronics

### 4.2.1. General layout

The electronics of the hodoscopes is similar for all the trigger subsystems and follows the layout shown in Fig. 12. Below we will discuss the case of the middle trigger which is the most complex one.

The horizontal strips of the hodoscopes H4MH and H5MH are read out on both sides via PMs. The signals are discriminated in CFDs. The digital signals from the CFDs are then fed into a meantimer which compensates the propagation time of the light in the scintillators as a function of the point of impact. The signals from the counters of the H4 hodoscope and those of the H5 hodoscope enter a coincidence matrix, which allows to select (in the case of the horizontal counters) hit combinations belonging to tracks originating from the target. The vertical strips

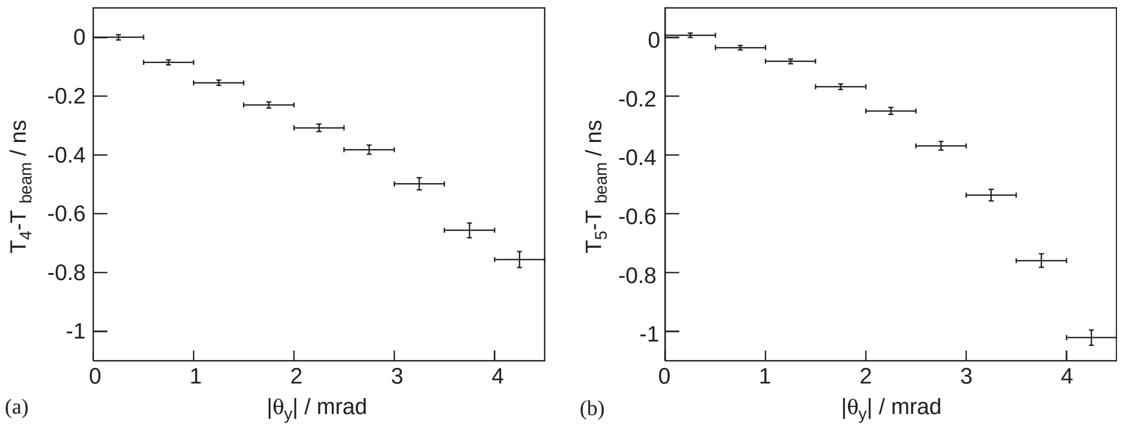

Fig. 10. Mean of the difference of the (a) H4I and (b) H5I time and the time of the beam track vs $\theta_y$ averaged over all elements.

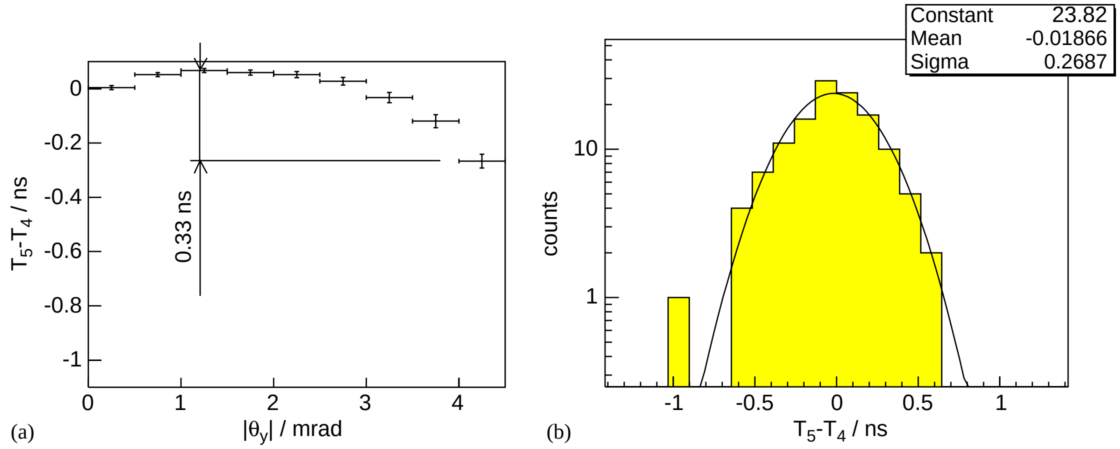

Fig. 11. (a) Mean of $\Delta t = T5 - T4$ vs $\theta_y$ averaged over all elements, (b) distribution of $\Delta t$ for single elements compared to a fit with a Gaussian distribution with a $\sigma$ of 270 ps.

have only one photomultiplier attached and no meantimer stage. The CFD outputs are directly interfaced to a coincidence matrix, which selects hit patterns according to the energy loss of the tracks (see Section 3).

The outputs of the "vertical" and "horizontal" matrices are then combined in a coincidence unit to form the hodoscope trigger, which provides the input to the last stage of the trigger logic. The signal from the calorimetric part of the trigger and the veto are added in an additional coincidence unit to form the trigger candidate.

The other trigger subsystems have a somewhat simpler electronics: the inner trigger has only vertical elements and no veto for halo contributions is applied; the ladder trigger has vertical elements with mean timers and only part of the veto ($V'$ in Section 4.4); the outer trigger has only horizontal strips and veto but no coincidence with the calorimeter.

### 4.2.2. *Components of the electronics*

Since about 1000 electronic channels are needed, custom designed modules have been produced. To

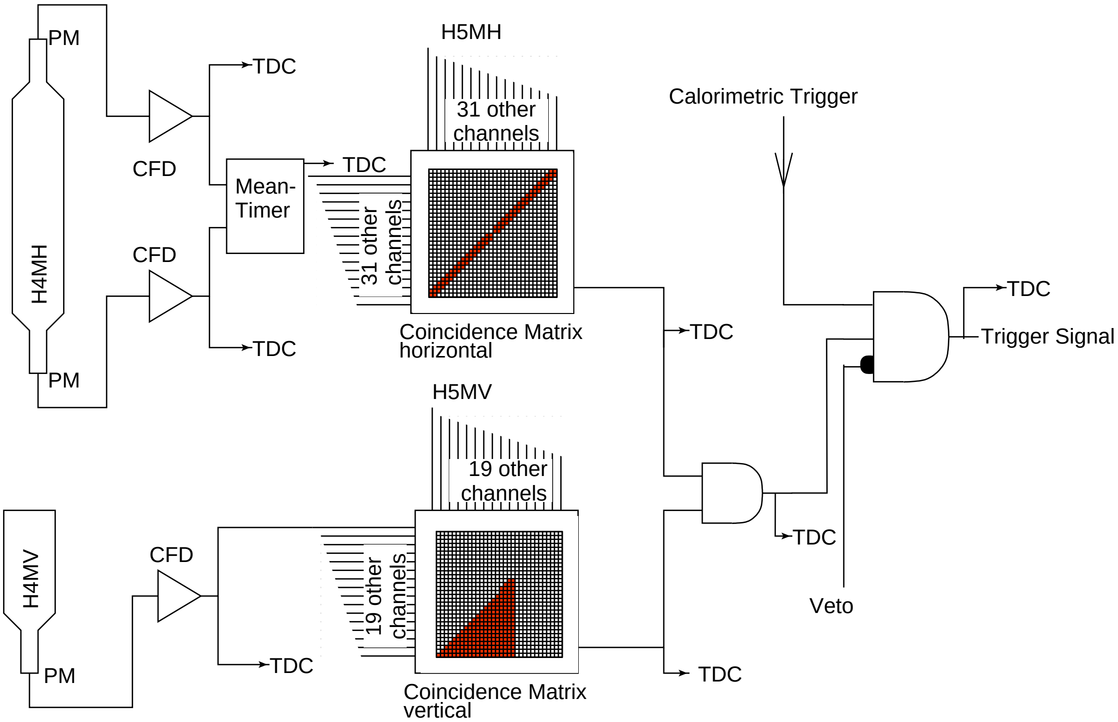

Fig. 12. Schematics of one channel of the middle trigger.

allow for a high packing density the discriminator/mean timer and the coincidence matrix stages are implemented with VME based electronics, interconnected by flat cables with 32 signal pairs. The rest of the electronics is realised with conventional NIM modules.

*Discriminators*. We make use of discriminator modules developed by the IPN Orsay, each of which contains two CFDs and one optional mean timer. 32 of these modules are mounted to a 9U VME board. Thus one board can handle up to 32 double sided counters or 64 single sided counters (see Table 2).

The CFDs employ one comparator for threshold discrimination, and another one which compares the differentiated with the integrated signal for pulse height independent timing. The meantimer works with one current source per input to ramp a voltage across a capacitor up to a threshold level [13]. This allows to choose the delay and the range of the mean timing stage as needed. The VME bus allows to set the threshold and the delay for each CFD channel individually and also to set the delays for the meantimers.

Table 2
Parameters of the discriminator boards

| | Meantimer-mode | Single-end mode |
|---|---|---|
| Number of channels | 32 | 64 |
| Outputs per channel | 4 MT, 1 for each end | 3 |
| Threshold resolution | 7.8 mV (2V in 256 steps) | |
| Double pulse resolution | 30 ns + MT delay | 20 ns |

*Coincidence matrices*. The matrices are built as 6U VME boards and allow the observation of coincidences between 32 rows and 32 columns of inputs with each of the 1024 coincidence units separately switchable (see Fig. 13). In order to be able to suppress accidental coincidences a short time window is needed, which requires to time-in all the 64 input channels of one matrix. A very low timing skew between the individual coincidence signals is necessary. To meet this requirement a full custom matrix chip was developed.

The programmable delay and pulse shaping was implemented in the form of a fully custom designed CMOS chip, which provides 16 individual channels, each with a 32 step delay with a 9 ns range and pulse lengths of up to 8 ns. These delay units are implemented as inverter chains, using the propagation delays of the inverters. Five chains with 2, 4, 8, 16 and 32 inverters can be combined, making up $2^5$ steps of the delay. For the pulse shaping part of each channel one such delay unit is employed to set the pulse length, which determines the coincidence time window.

The boards and their components can be tested by software using the basic parts of a boundary scan interface [14] implemented into both the matrix and the delay chips. This feature provides an efficient way to test the chips and board assembly.

### 4.2.3. Setup and performance

The matrix patterns are determined from the known geometry and the desired acceptance in $y$. Timing corrections and optimal pulse lengths must be set to account for the differences in the timing of the individual hodoscope elements. To do so, special runs are taken in which the delay for one of the two hodoscopes connected to one matrix board is fixed in the middle of the available range, while the other is stepped through the full range. In this way, the timings for a sufficient number of matrix elements can be determined and from them the optimum delay settings for both hodoscopes can be calculated.

With all the delays set to their optimal values, the overall performance of the system can be checked by a variation of the pulse widths at the input of a coincidence matrix. Fig. 14 shows the result of such a pulse width scan for a pair of hodoscopes. A steep rise of the output rate is

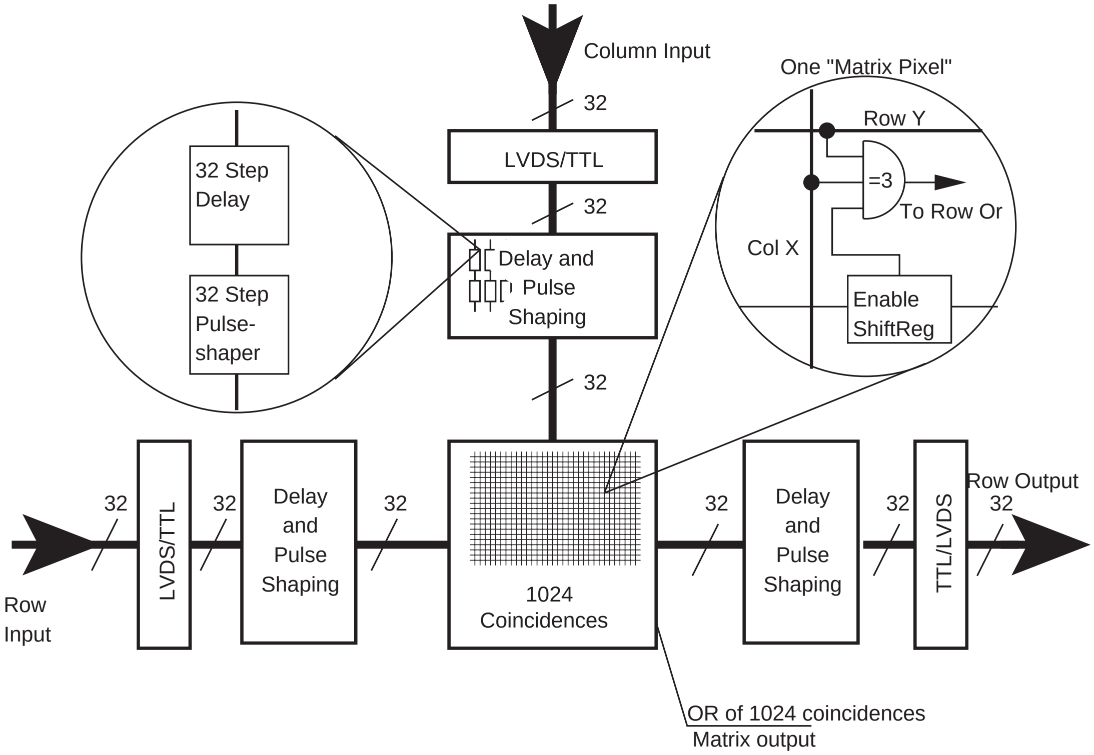

Fig. 13. Schematics of the matrix board.

observed for a pulse width larger than 1.2 ns, the minimal width required by the coincidence unit. Saturation is reached at 2 ns. The output rate rises slowly for pulse lengths longer than 2 ns due to random coincidences. The steep rise within 1 ns is expected for correctly adjusted delays of the inputs and the time resolution observed between two hodoscope elements as shown in Fig. 11b.

### 4.2.4. Pulser system

To reduce the setup time and improve the monitoring of the trigger system a pulser system was developed. A small test setup attached to the middle trigger system has already been used in 2003. To simulate muon signals ultra bright blue (470 nm) pulsed LEDs are used and the light pulses fed via optical fibers into the scintillators. The time jitter between the trigger pulse and the light pulse is less than 250 ps. Correlated light pulses in several scintillators are obtained by generating trigger pulses using the same delay chips as in the matrix boards. The time difference between two correlated pulses can be adjusted between 0 and 40 ns. Delay curves were measured by monitoring the common OR matrix output of the middle trigger system during spill pauses. They were found to be stable within 200 ps over a time of several months.

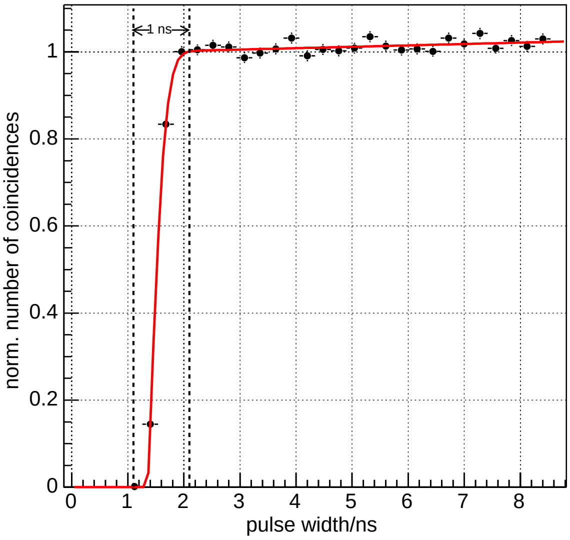

Fig. 14. Pulse width scan of a pair of hodoscopes. Shown is the sum of all matrix elements. The line is meant to guide the eye.

## 4.3. The calorimetric trigger

Muon scattering events with a hadronic energy exceeding a certain threshold are tagged by the response of the hadron calorimeters. As pointed out in Chapter 3.2 a threshold has to be set for an effective suppression of muon tracks. The minimal hadron energy deposit has to exceed this threshold in at least one cluster sum. For good purity of the combined trigger, the rate of accidental coincidences between the muon candidates seen by the hodoscope system and the hadron signals in the calorimeters have to be minimized by optimizing the calorimeter time resolution.

The COMPASS experiment uses two iron-scintillator sandwich calorimeters with a thickness of $5\lambda_{\mathrm{int}}$ to cover large angles (HCAL1 50–150 mrad) [15] and forward angles (HCAL2 5–50 mrad). Both are read out by wavelength shifter fibers or plates coupled to FEU-84A photomultipliers. The module size is $15 \times 15\,\mathrm{cm}^2$ for HCAL1 and $20 \times 20\,\mathrm{cm}^2$ for HCAL2. Both are positioned behind an electromagnetic calorimeter or shielded by a lead wall of an equivalent number of radiation lengths. There are 480 modules in HCAL1 (Fig. 15) and 216 in HCAL2 (Fig. 16). The calorimeter signals have rise times of typically 10 ns. A time resolution of $\sigma_{\mathrm{t}} = 1.4\,\mathrm{ns}$ was obtained for signals above threshold. To reach such a time resolution for a dynamical range of about 4–80 GeV hardware walk compensation was applied at the trigger level.

The distribution of single muon signals as measured with an integrating (80 ns) ADC is shown in Fig. 17. It exhibits a maximum equivalent to the most probable energy loss of 1.8 GeV. In order to reject more than 90% of the muons a threshold of 3 times the typical muon response is set. This choice also rejects hadrons with energies lower than about 6 GeV. To obtain high efficiency for hadrons with energies beyond this threshold it is necessary to sum up the energy of the hadron shower which is spread over a number of calorimeter modules. The region which is summed over has to be close to the lateral shower extension to minimize noise and pile up with halo muons. For practical reasons we sum over a region of 4 × 4 modules.

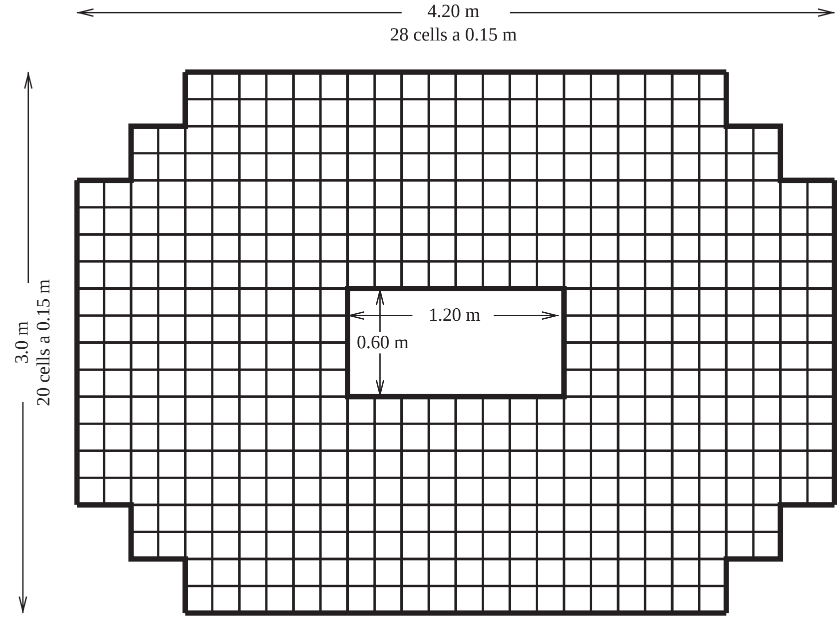

Fig. 15. Shape and distribution of the 480 cells of HCAL1. The 2 × 2 modules summed in the first stage are indicated by thick lines.

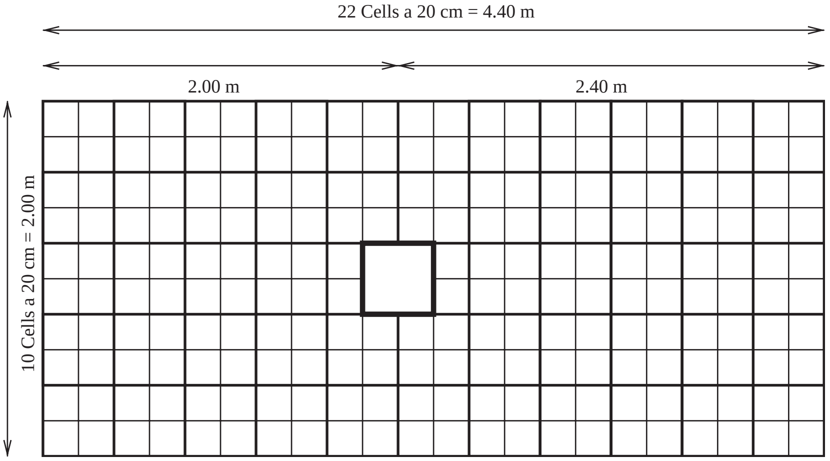

Fig. 16. Shape and distribution of the 216 cells of HCAL2. The beam hole which is not in the centre corresponds to 4 cells ($40 \times 40\,\mathrm{cm}^2$). The grouping of cells into 2 × 2 modules is indicated by thick lines.

The schematic layout of the custom built electronics is illustrated in Fig. 18. In order to avoid disturbing the readout of the calorimeter modules by fast integrating ADCs, 5% of the PM output signal height is divided passively for trigger purposes in a splitter unit. Each of these units handles 16 calorimeter modules. The number of signals for the trigger system is reduced by summing the response of 2 × 2 calorimeter modules to generate the "sum-of-4" signals. These signals are transmitted by twisted pair cables to the trigger control room at a distance of 25 m. The

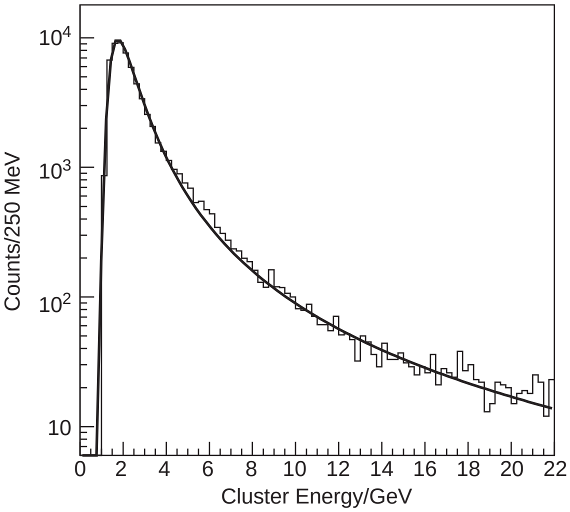

Fig. 17. The distribution of the energy deposition of single muons in a 3 × 3 cluster of HCAL1. The spectrum is fitted with a Landau distribution. The most probable energy loss is 1.8 GeV.

sum-of-4 signals are then processed further to form "sum-of-16" signals corresponding to 4 × 4 calorimeter modules. Pulse height discrimination and constant fraction timing is provided for each of these signals.

The summation/discriminator boards in the trigger control-room have eight identical summation units with two discriminators. Each unit takes four sum-of-4 symmetrical signals to form a sum-of-16 cluster sum. It is fed into two CFDs with adjustable computer controlled thresholds. The output (MECL) of the two discriminators is fed to a MECL-LVDS converter and from there to the TDCs. Each board produces 8 threshold-1 and 8 threshold-2 signals. The 8 digital signals corresponding to each of the two thresholds are summed, each active output adding 50 mV to the sum signal. These two signals are fed into two leading edge discriminators with computer controlled threshold to provide an "OR" or a "multiplicity-*n*" signal for threshold-1 and threshold-2.

The arrangement of calorimeter modules into neighbouring, not-overlapping 4 × 4 groups for summation and energy discrimination is called logical layer. A single logical layer is not efficient for hadrons hitting the edge of a 4 × 4 module. By shifting the first logical layer by 2 modules sidewards and downwards one additional logical layer is formed (see Fig. 19). Two more layers are formed by shifting the first one downwards or sidewards by two modules. With four logical layers all hadron showers will be covered by at least one sum-of-16 signal. For the HCAL1 calorimeter with 480 modules, one logical layer consists of 30 sum-of-16 cluster signals. Four summation/discriminator boards are used for one logical layer. In order to form the four different logical layers (as indicated in Fig. 19), the original 2 × 2 signals are split into four identical symmetrical signals. The patterns necessary to form the layers are realized on a passive signal distribution board. From the 4-fold splitters on these boards, short twisted pair cables are used to form the different combinations which are then fed into the summation boards.

The sum of the logical signals can also be fed into neighbouring boards to provide larger units. The multiplicity unit is only used on the "master" board. The other boards feed their summed logical signals into the master board. The output of the multiplicity unit is used to form the calorimetric trigger. The 4 layers work independently to form their trigger. The logical OR of the multiplicity-1 signals from each layer are ORed together to form the trigger for this calorimeter. Fig. 20 shows the TDC spectrum of the HCAL1 signal relative to the ladder hodoscopes (left), the time resolution is about 1.4 ns. The single cell TDC spectrum (right) has a time resolution of about 1 ns.

In the current setup the second threshold is used for a standalone calorimetric trigger at 16.2 GeV equivalent to 9 times the typival muon response. This allows us to take data with a trigger independent of the hodoscope system. The purpose of this trigger is twofold: it extends the kinematical range to large $Q^2$ values not covered by the hodoscopes (see Fig. 25) and allows an evaluation of the hodoscope trigger efficiencies.

### 4.4. The veto system

The use of calorimeter information in the trigger decision may lead to a bias in the event selection, e.g. due to a difference in the acceptance for

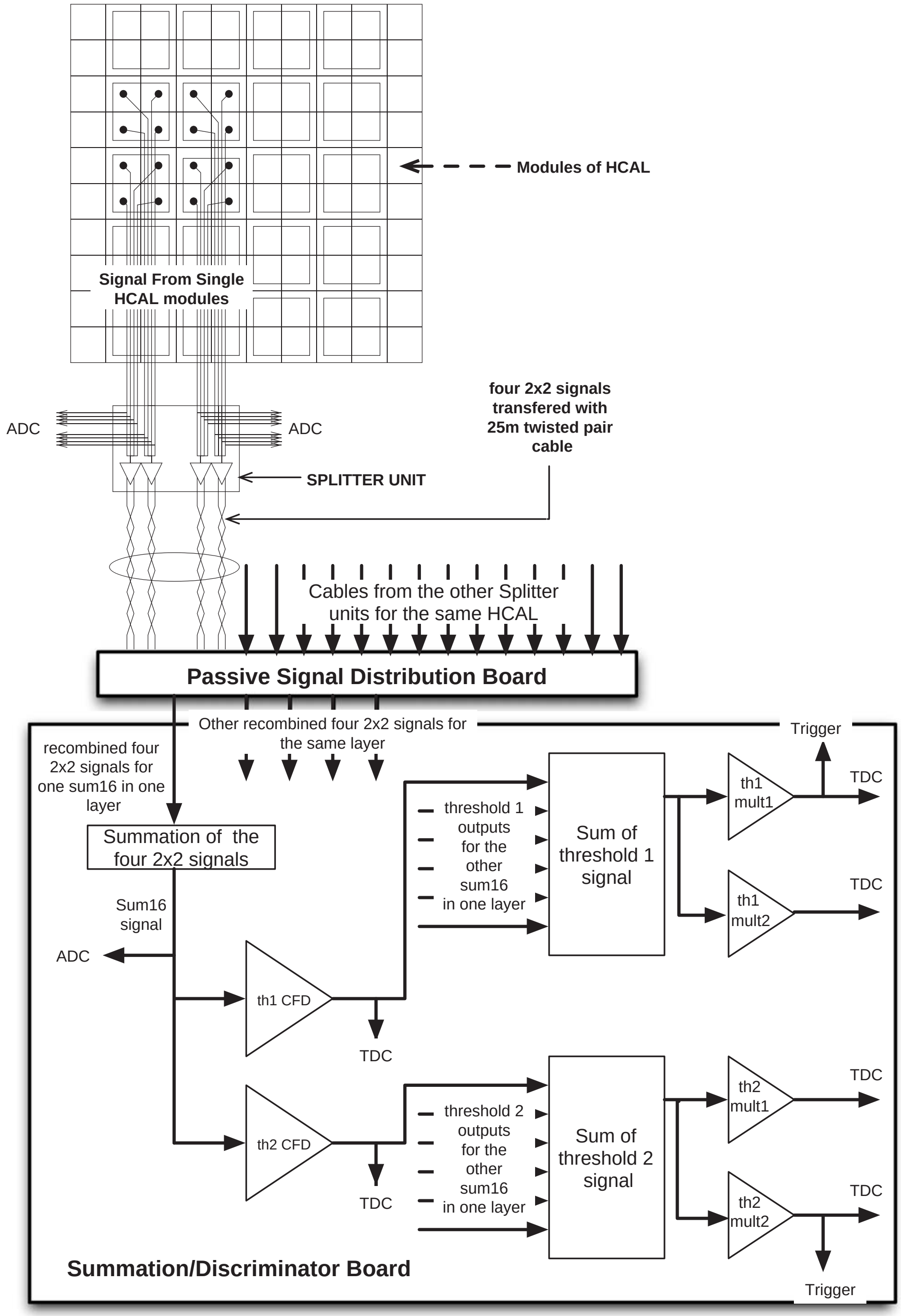

Fig. 18. The schematic layout of the calorimeter electronics.

positive and negative hadrons. It would thus be desirable to avoid using this information for the measurement of inclusive spin asymmetries. However, a trigger based only on a coincidence between two hodoscope planes would result in a rate of the order of $10^6$ per spill, much too high for the DAQ system. Most of these coincidences are caused by halo muons not interacting in the target. They can be rejected by a veto system (see Fig. 21) which has been added to the trigger. It consists of hodoscopes upstream the target, leaving the central region around the beam uncovered. A large fraction of the unwanted trigger signals can be eliminated by demanding the absence of a signal in the veto system together with a coincidence in two hodoscope planes.

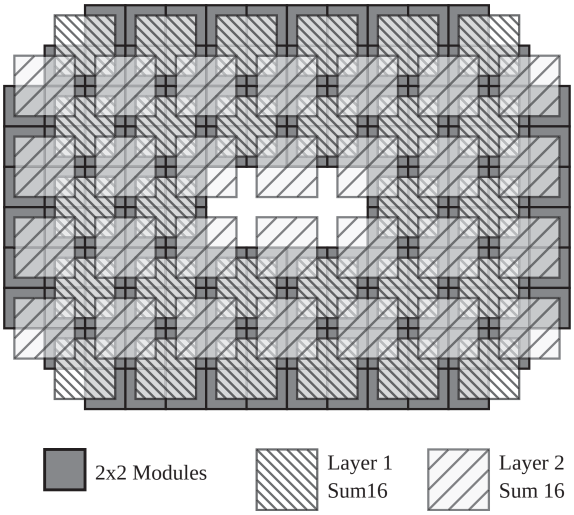

Fig. 19. The grouping of the 2 × 2 module signal into sum-of-16 signals of the first two layers of HCAL1 is shown.

The first hodoscope of the veto system, $\text{Veto}_1$, is located at $z_{\text{V1}} = -800\,\text{cm}$ and the second smaller one, $\text{Veto}_2$, at $z_{\text{V2}} = -300\,\text{cm}$. Two veto hodoscopes at different positions along the beam are needed to veto divergent beam particles passing through the hole in one of them, as illustrated in Fig. 21. In the middle trigger, for instance, the application of $\text{Veto}_1$ or $\text{Veto}_2$ alone reduces the rate to 9% and 46%, respectively, whereas the combination $\text{Veto}_1 + \text{Veto}_2$ leads to 4% of the rate without veto. The acceptance of the middle trigger starts at 4 mrad in the non-bending plane. The veto system is only fully efficient for tracks with a slope greater than 8 mrad, the ratio of the inner hole diameter to the distance $z_{\text{V2}} - z_{\text{V1}}$. A smaller diameter of the inner hole and/or a larger distance between $\text{Veto}_1$ and $\text{Veto}_2$ would be beneficial to veto tracks with an angle smaller than 8 mrad as well. The minimal size of the inner hole is limited by the target diameter of 3 cm and dead time losses discussed below. The maximum distance between $\text{Veto}_1$ and $\text{Veto}_2$ is determined by the space available between the last beam-line element and the target. To be able to veto tracks passing

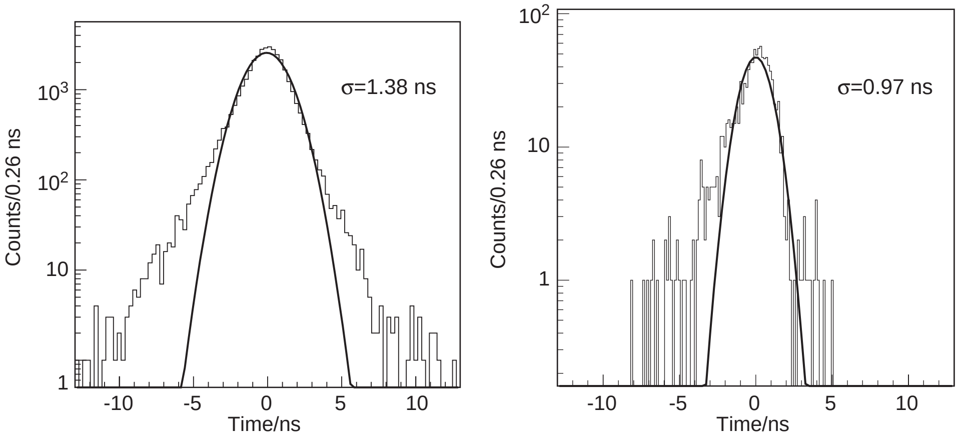

Fig. 20. TDC spectrum of the HCAL1 trigger signal relative to the ladder hodoscopes (left), TDC spectrum for a single module in HCAL1 (right).

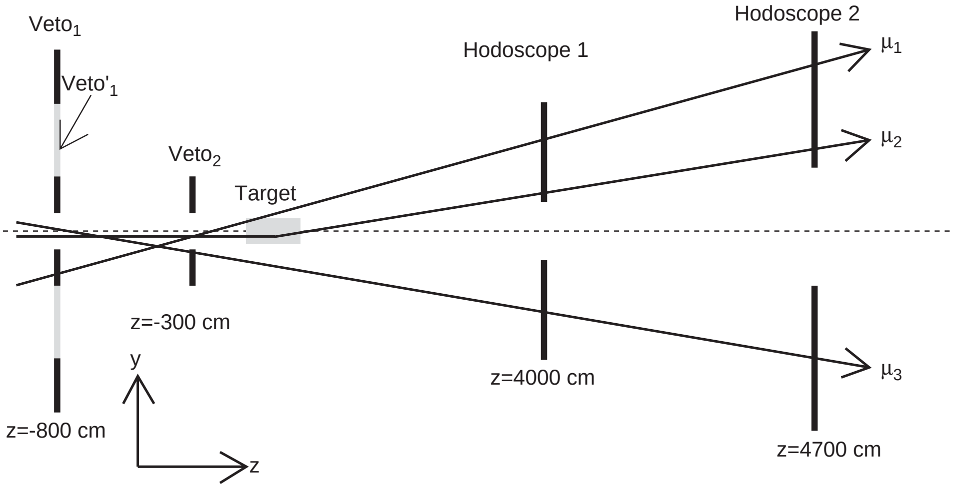

| | Dimensions/ cm | $z$-pos./ cm | no. of elements | dead time/ % | Rate/ MHz |
|---|---|---|---|---|---|
| single Hodoscopes | | | | | |
| Veto$_1$ | 250×320, ○ 4 | -800 | 34 | 16 | 8.2 |
| Veto'$_1$ | 250×120 ,□ 30×30 | -800 | 24 | 1.7 | 4 |
| Veto$_2$ | 30×30, ○ 4 | -300 | 4 | 5.9 | 9 |
| V$_{\mathrm{bl}}$ | 50×50, □ 10×10 | -2000 | 4 | 1.9 | 4 |
| combinations | | | | | |
| V' = Veto'$_1$ + $V_{\mathrm{bl}}$ | | | | 6 | 2.9 |
| V$_{\mathrm{tot}}$ =Veto$_1$ + Veto$_2$ + $V_{\mathrm{bl}}$ | | | | 21 | 14.7 |

Fig. 21. Schematical layout of the veto system. The tracks $\mu_1$ and $\mu_3$ are vetoed, whereas the track $\mu_2$ fulfills the inclusive trigger condition. In column 2 the outer dimensions and the diameters/sizes of the inner holes are given. The symbol ○ stands for a circular, □ for a quadratic hole. $V_{\mathrm{bl}}$ is the additional veto hodoscope placed further upstream in the beam line to veto tracks passing through both holes in Veto$_1$ and Veto$_2$, Veto$'_1$ is part of Veto$_1$.

through both holes in Veto$_1$ and Veto$_2$ a third veto hodoscope, $V_{\mathrm{bl}}$, was placed further upstream in the beam line at $z = -2000$ cm. Its inclusion in the veto condition leads to a further reduction of the rate to 1.4% for the middle trigger. The veto hodoscopes are segmented into several scintillator elements: smaller elements with better time resolution are used close to the beam axis and larger elements in the outside region.

A drawback of a veto system is the dead time associated to it. It is given by the product of the rate of the system, $R_{\mathrm{Veto}}$, and the duration of the time gate, $T_{\mathrm{Veto}}$, during which the veto prohibits a trigger signal. The minimal time gate $T_{\mathrm{Veto}}$ is given by the time jitter of both the veto and the trigger hodoscopes. The segmentation of the veto counters allows one to select individual time windows for the different elements to minimize the dead time. Fig. 22 shows two time spectra of the veto system with respect to the trigger time, one of them taken with the veto included in the trigger, the other one when it was not. The value of $T_{\mathrm{Veto}}$ was

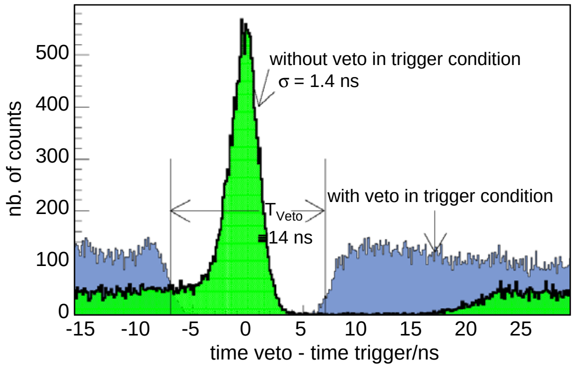

Fig. 22. Time spectra of the veto system with respect to the trigger time. The depletion on the rhs of the peak is due to the double pulse resolution of the discriminators for the veto signals. The normalization of the two distributions is arbitrary.

chosen to be $\pm 5\sigma$ where $\sigma = 1.4\,\text{ns}$ is the time resolution of the veto system with respect to the trigger. The losses due to dead time of the full veto system $V_{\text{tot}} = \text{Veto}_1 + \text{Veto}_2 + V_{\text{bl}}$ are 21% at nominal beam intensity. A subsample of the veto elements was used to form a veto signal $V' = \text{Veto}'_1 + V_{\text{bl}}$ with a smaller reduction factor and dead time losses reduced to 6%.

Table 3 shows the trigger counts per spill for various triggers and veto configurations. For the inclusive triggers (middle and outer) the application of $V_{\text{tot}}$ leads to a reduction of the rate by approximately two orders of magnitude. For the low $Q^2$ triggers (inner and ladder) a veto should not be necessary if in addition to the hodoscope coincidence a calorimeter signal is included in the trigger condition. This statement is true for the inner trigger, where $V_{\text{tot}}$ reduces the trigger rate only to 50%. For the ladder trigger, however, the situation is different: the ladder hodoscopes overlap with the calorimeters (see Fig. 5), so that a halo muon may traverse HCAL2 and both hodoscopes. If the muon energy deposition exceeds the threshold this event will fulfill the trigger condition. This class of events can be rejected by the veto system. To avoid large dead-time losses only $V'$ is applied.

Table 3
Trigger counts in 1000/spill for different trigger configurations

| | | $\overline{V'}$ | $\overline{V_{\text{tot}}}$ | Calo | Calo $\times\overline{V'}$ | Calo $\times\overline{V_{\text{tot}}}$ |
|---|---|---|---|---|---|---|
| Inner | 1049 | 513 | 219 | **11** | 8 | 5 |
| Ladder | 564 | 114 | 34 | 26 | **6** | 3 |
| Middle | 1400 | 120 | **20** | 50 | 4 | **1** |
| Outer | 899 | 28 | **8** | 54 | 2 | 0.6 |
| Calorimeter | 106 | 27 | **5** | — | — | — |

The trigger conditions chosen during the data taking are shown in bold face. The beam intensity was $2 \times 10^8$ muons per spill. $V_{\text{tot}} = \text{Veto}_1 + \text{Veto}_2 + V_{\text{bl}}$, $V' = \text{Veto}'_1 + V_{\text{bl}}$.

The efficiency of the veto system, $\varepsilon$, can be estimated knowing the trigger rate with (20000) and without veto ($1.4 \times 10^6$) and the purity of the trigger, discussed in Section 5. For the middle trigger the estimated purity is 0.15. From these number one deduces an efficiency of

$$\varepsilon = \frac{\text{vetoed muons}}{\text{muons which should be vetoed}} = \frac{1400000 - 20000}{1400000 - 0.15 \cdot 20000} = 0.988.$$

A compromise must be found between a lowest possible bias (i.e. no calorimeter in the trigger), low losses due to dead time (i.e. no veto in the trigger) and the maximum rate compatible with the data acquisition (DAQ) system (50000 triggers/spill). This compromise results in the selection of trigger conditions shown in bold face in Table 3. Two different triggers are derived from the middle trigger system, one without and one with requiring a coincidence with the calorimetric trigger. This allows one to evaluate the efficiency of the calorimetric trigger.

## 5. Results

The performance of the trigger system has been studied in detail on the 2002 and 2003 data. The efficiency of the hodoscope triggers has been determined with help of the standalone calorimetric trigger. Using offline reconstructed events with an incoming and a scattered muon one can predict whether the scattered muon fulfills a given matrix pattern. The ratio of the number of events selected by a specific trigger to the predicted one yields the efficiency of the whole subsystem. This includes the scintillator material, light coupling,

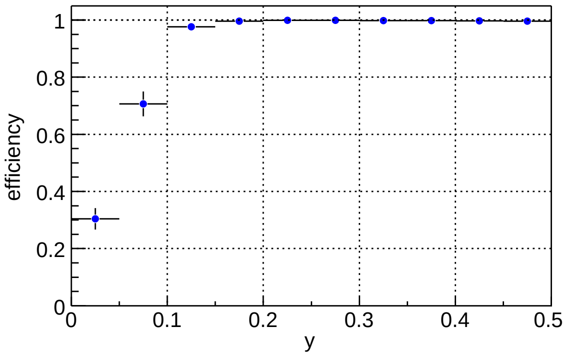

Fig. 23. The efficiency of the lower part of the inner trigger system as a function of the relative energy loss $y$.

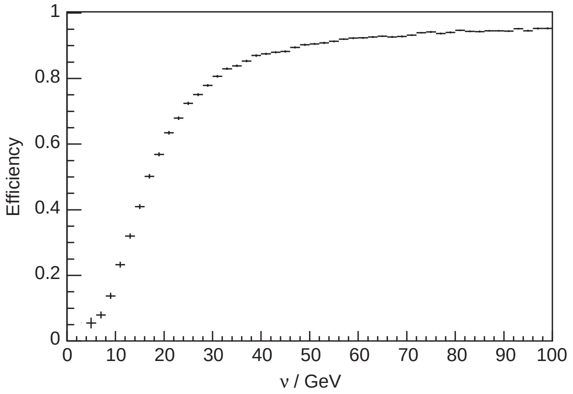

Fig. 24. Efficiency of the calorimetric trigger for HCAL1 and HCAL2 vs the muon energy loss using a threshold of 5.4 GeV.

photomultiplier, readout electronics and the setting of the matrix timing.

Due to the good performance of the calorimetric trigger it was possible to use a very low $y_{\min}$ for the inner trigger system. A pattern was loaded during data taking resulting in close to 100% efficiency for $y > 0.2$ as can be seen in Fig. 23 for the lower part. Events with low $y$ are suppressed as intended.

The global efficiencies for all 4 subsystems were determined with the same method and yield values of above 99% for the inner and the ladder system, >97% for the middle and >96% for the outer system. These lower numbers are due to the suppression of trigger matrix elements which are affected by large backgrounds compared to the signal.

The efficiency of the calorimetric trigger has been studied in a similar way, using events with more than three reconstructed outgoing tracks at the main vertex from the middle trigger (without calorimeter condition). The obtained dependence of the efficiency on the muon energy loss is shown in Fig. 24 for a threshold of 5.4 GeV. At $\nu \approx 40\,\mathrm{GeV}$ an efficiency of about 90% is reached.

The kinematical range covered by the trigger system is illustrated in Fig. 25. It shows the measured event distribution in $y$ and $Q^2$ for the four hodoscope trigger subsystems. Events with small $Q^2$ (quasi-real photon events) are selected by the inner and ladder systems. The cut at low $y$ of between 0.1 and 0.15 is clearly visible for the inner trigger. Together with the ladder trigger the whole $y$ range from 0.2 to 0.9 is covered for small $Q^2$. The middle and outer trigger mainly select deep inelastic events up to $Q^2 \approx 20\,\mathrm{GeV}^2$. The range can be further extended towards high $Q^2$ with the help of the standalone calorimetric trigger.

The effect of requiring the calorimetric trigger in coincidence with the hodoscope triggers is illustrated in Fig. 26 for the $x_{\mathrm{Bj}}$ dependence of the middle trigger events. The prominent peak at $x_{\mathrm{Bj}} = m_{\mathrm{e}}/m_{\mathrm{p}}$ is due to elastic muon electron scattering events. The light grey distribution is obtained using the middle trigger without calorimeter condition. Applying the calorimetric trigger results in the dark grey distribution. As can be seen the elastic muon electron scattering events are efficiently suppressed. The remaining events in the peak region are due to random coincidences. The differences between the two distributions are consistent with the efficiency of the calorimetric trigger shown in Fig. 24.

Purities for the different trigger subsystems can be estimated from the ratio of the number of triggered events reconstructed with a vertex with an incoming and a scattered muon, to the total number of triggered events. Corrections for the beam and scattered muon reconstruction efficiency have been applied. The purities are approximately 35% for triggers including calorimetric information and 15% for the inclusive triggers. As the precision of the $\Delta G$ measurement is limited by

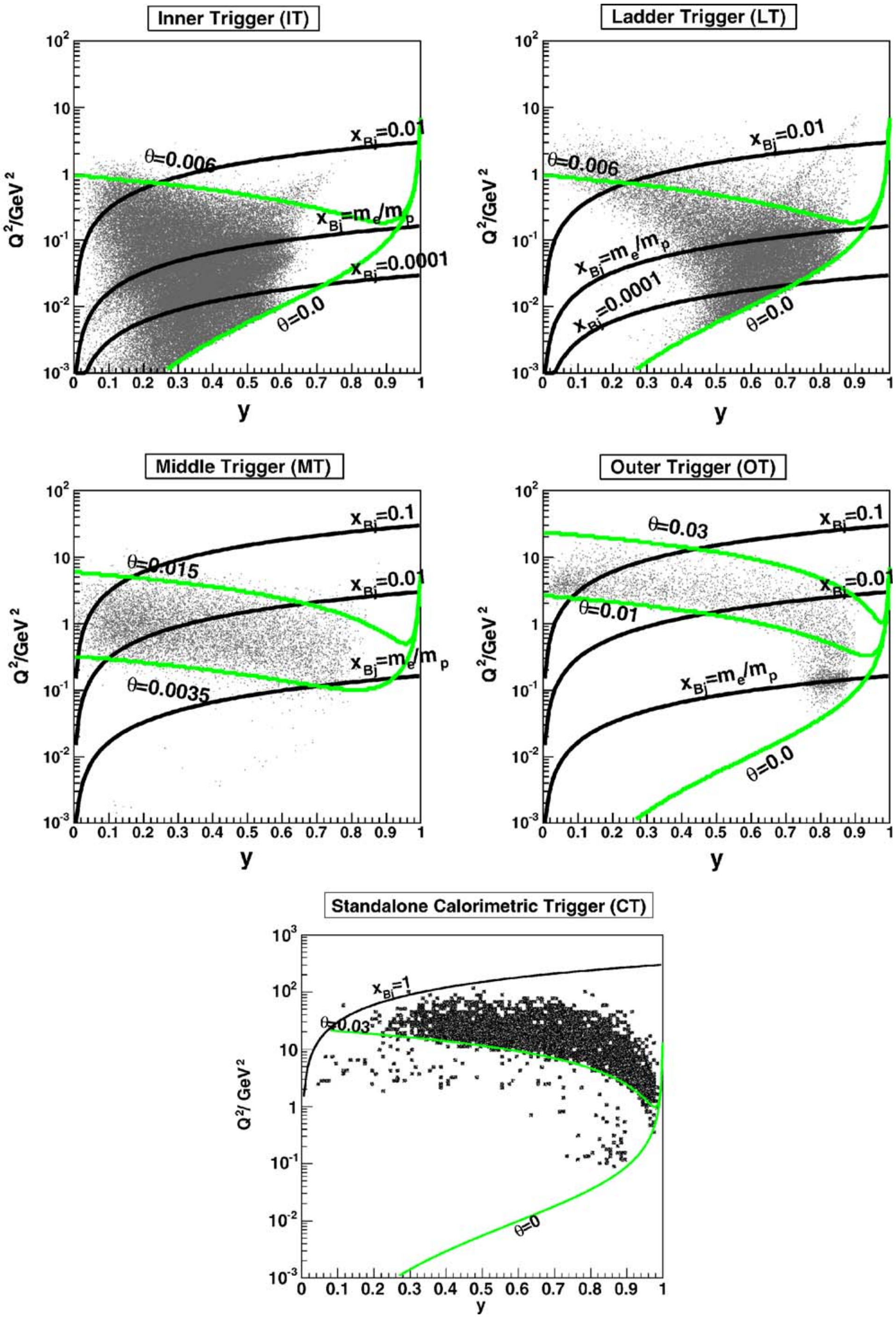

Fig. 25. Event distribution in $y$ and $Q^2$ for the four hodoscope trigger subsystems and the standalone calorimetric trigger, $\theta$ is the muon scattering angle in the laboratory system. Here, the inner, ladder and middle trigger were used with calorimeter condition, events with an additional hodoscope trigger were excluded for the calorimetric trigger.

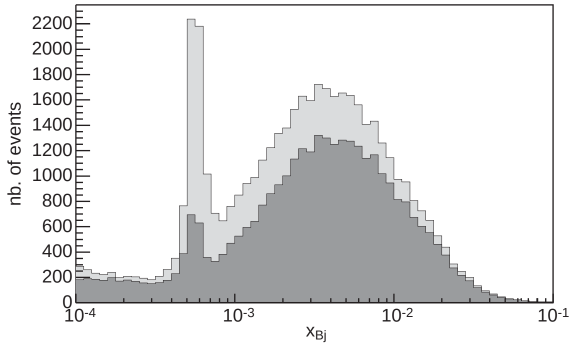

Fig. 26. The $x_{\mathrm{Bj}}$ distribution of events selected by the middle trigger without (light grey) and in coincidence with the calorimetric trigger (dark grey). The peak at $x_{\mathrm{Bj}} = m_{\mathrm{e}}/m_{\mathrm{p}} = 1/1836$ corresponds to $\mu$-e elastic scattering.

statistics, high efficiencies are mandatory even at the expense of lower purities.

To increase the purity, online filtering of the digitized data is planned. For this purpose part of each event is decoded and processed in real time. The time available per event is about 40 ms which is enough time to apply simple algorithms e.g. to check the presence of a beam candidate. The filter [16] has been used at the end of 2003 data taking and rejected 20% of the triggered events.

## 6. Summary

A trigger system for muon interactions has been set up for the COMPASS experiment. Using a novel scheme for triggering quasi-real photon events with a freely adjustable minimum energy loss as well as deep inelastic events are selected. Thus, the acceptance is extended towards lower $x$ and $Q^2$ compared to previous muon experiments to record photon gluon fusion events in the largest possible kinematical range.

The main new component of the trigger system is the inner trigger system for quasi-real photon events which selects scattered muons with a certain minimum energy loss together with a fast calorimetric trigger rejecting non-hadronic final states.

A compact and flexible trigger electronics has been developed on the basis of custom CMOS chips. Precision timing for tight coincidence conditions is achieved by computer controlled delays and an automatic optimisation procedure. Fast analog cluster processing of hadron calorimeter information is implemented on the trigger level.

The system has been used for data taking since 2002. A good performance with respect to efficiency and stability was achieved for all trigger subsystems. For the coming years main emphasis will be on the improvement of the monitoring of the whole trigger system and further developments of the online filter.

## Acknowledgments

We are grateful to a many people who have been involved in the construction of this trigger system. In particular we wish to thank: M. Henseler (Bonn) for his design work for the matrix chips and the matrix and discriminator boards, B. Neff (Bonn) and R. Loos (CERN) for the help in the construction of the trigger hodoscopes, G. Stefan (Mainz) for his work in the design and production of PM bases, K. Weindel (Mainz) for his contribution to the calorimeter trigger electronics, and R. Sellem and M. Engrand (IPN Orsay) for their design and advice for the discriminator modules.

## References

[1] T. Sloan, G. Smadja, R. Voss, Phys. Rep. 162 (1988) 45.
[2] E665, M.R. Adams et al., Phys. Rev. D54 (1996) 3006.
[3] EMC, J. Ashman et al., Nucl. Phys. B321 (1989) 541.
[4] SMC, D. Adams et al., Phys. Rev. D56 (1997) 5330.
[5] EMC, O. Allkofer et al., Nucl. Instr. and Meth. 179 (1981) 445.
[6] For more details see: http://wwwcompass.cern.ch/compass/detector/trigger/muon-trigger
[7] G. Mallot, Nucl. Instr. and Meth. A518 (2004) 121 COMPASS Collaboration, Compass proposal, CERN/SPSLC 96-14, SPSC/P297, CERN/SPSLC 96–30, 1996.
[8] N. Doble et al., Nucl. Instr. and Meth. A343 (1994) 351.
[9] J. Ball et al., Nucl. Instr. and Meth. A498 (2003) 101.
[10] E. Albrecht et al., Nucl. Instr. and Meth. A502 (2003) 112 and references therein.
[11] M. Leberig, Ph.D. Thesis, Mainz, 2002.
[12] K. Grimm, Ph.D. Thesis, Mainz, 2002.

[13] A.R. Baldwin, R. Madey, Nucl. Instr. and Meth. 171 (1980) 149.

[14] IEEE Standard 1149. 1–1990. IEEE Standard Test Access Port and Boundary-Scan Architecture, IEEE, June 1989.

[15] O. Gavrishchuk et al., Preprint JINR D13-2004-186, Dubna, 2004.

[16] R. Kuhn, private communication;
T. Nagel, Diploma Thesis, TU München, 2004.